

EVIDENCE FOR NUCLEAR RADIO JET AND ITS STRUCTURE DOWN TO  $\lesssim 100$  SCHWARZSCHILD RADII  
IN THE CENTER OF THE SOMBRERO GALAXY (M 104, NGC 4594)KAZUHIRO HADA<sup>1,2</sup>, AKIHIRO DOI<sup>3</sup>, HIROSHI NAGAI<sup>2</sup>, MAKOTO INOUE<sup>4</sup>,  
MAREKI HONMA<sup>2,5</sup>, MARCELLO GIROLETTI<sup>1</sup>, AND GABRIELE GIOVANNINI<sup>1,6</sup><sup>1</sup>INAF Istituto di Radioastronomia, via Gobetti 101, I-40129 Bologna, Italy<sup>2</sup>National Astronomical Observatory of Japan, Osawa, Mitaka, Tokyo 181-8588, Japan<sup>3</sup>Institute of Space and Astronautical Science, Japan Aerospace Exploration Agency, 3-1-1 Yoshinodai, Chuo, Sagami-hara 252-5210, Japan<sup>4</sup>Academia Sinica Institute for Astronomy and Astrophysics, 11F Astronomy-Mathematics Bldg., National Taiwan University, No. 1, Roosevelt Rd., Sec. 4 Taipei 10617, Taiwan R.O.C.<sup>5</sup>Department of Astronomical Science, The Graduate University for Advanced Studies (SOKENDAI), 2-21-1 Osawa, Mitaka, Tokyo 181-8588, Japan and<sup>6</sup>Dipartimento di Fisica e Astronomia, Università di Bologna, via Ranzani 1, I-40127 Bologna, Italy

Draft Version

## ABSTRACT

Sombrero galaxy (M 104, NGC 4594) is associated with one of the nearest low-luminosity active galactic nuclei (LLAGN). We investigated the detailed radio structure of the nucleus of the Sombrero using high-resolution, quasi-simultaneous, multi-frequency, phase-referencing Very-Long-Baseline-Array observations. We obtained the VLBI images toward this nucleus, with unprecedented sensitivities and resolutions, at the seven frequencies between 1.4 and 43 GHz, in which those at 15, 24 and 43 GHz are the first clear VLBI detections and imaging for this source. At 43 GHz, where the highest resolution is available, the nuclear structure was imaged on a linear scale under 0.01 pc or 100 Schwarzschild radii, revealing the compact radio core with a high brightness temperature of  $\gtrsim 3 \times 10^9$  K. For the first time, we have discovered the presence of the extended structure in this nucleus, which is directing from the radio core in two sides toward northwest/southeast directions. The nuclear structure shows a clear spatial gradient on the radio spectra; the core region is mildly inverted whereas the extended region becomes progressively steep, as commonly seen in more luminous AGN with powerful relativistic jets. Moreover, the radio core shows a frequency-dependent size with an elongated shape toward the same direction of the extended structure, and the position of the radio core also tends to be frequency dependent. A set of these new findings provide evidence that the central engine of the Sombrero is powering radio jets, and the jets are overwhelming the emission from the underlying radiatively-inefficient accretion flow over the observed frequency range. Based on the observed brightness ratio of jet-to-counter jet, core position shift and its comparison with a theoretical model, we constrained the following fundamental physical parameters for the M 104 jets: (1) the northern side is the approaching jet, whereas the southern side is receding; (2) the inclination angle of the jet is relatively close to our line-of-sight, probably less than  $\sim 25^\circ$ ; (3) the jet intrinsic velocity is highly sub-relativistic at a speed less than  $\sim 0.2 c$ . The derived pole-on nature of the M 104 jet is in accordance with the previous argument that M 104 contains a true type II AGN, i.e., the broad line region of this nucleus is actually absent or intrinsically weak, if the plane of the presumed circumnuclear torus is perpendicular to the axis of the radio jets.

*Subject headings:* galaxies: active — galaxies: individual (M 104) — galaxies: nuclei — radio continuum: galaxies

## 1. INTRODUCTION

M 104 (NGC 4594) is a famous early-type spiral galaxy known as the “Sombrero”. It is located in the southern hemisphere at a distance of  $D = 9.0 \pm 0.1$  Mpc (Spitler et al. 2006) and the galactic plane shows a nearly edge-on view ( $84^\circ$  from our line-of-sight; Rubin et al. 1985). *Hubble Space Telescope* observations indicate the presence of a super-massive black hole weighing  $1 \times 10^9 M_\odot$  at the center (Kormendy et al. 1988, 1996). The nucleus is classified into a low-ionization nuclear emission region (LINER) based on its optical emission-line property (Heckman 1980), belonging to a representative sub-class of low-luminosity active galactic nuclei (LLAGN).

Physical processes acting in the vicinity of the LLAGN central engines remain as a major question in the local Universe (Ho et al. 1997a; Ho 2008, and the references therein). Because of the absence of the big blue bump and highly sub-Eddington luminosity in their spectral energy distributions (SED), the accretion state is thought to be described by

advection-dominated accretion flow (ADAF) or radiatively-inefficient accretion flow (RIAF), which is geometrically-thick and optically-thin with a hot electron temperature of  $\sim 10^9$  K (Narayan & Yi. 1994, 1995). Bremsstrahlung and inverse Compton emission from such flow reasonably explain the above characteristics of LLAGN SED as well as observed harder X-ray spectral nature (e.g., Manmoto et al. 1997; Narayan et al. 1998; Quataert et al. 1999). In contrast, observed LLAGN spectra at radio bands are typically flat or mildly inverted ( $\alpha < 0.2^1$ ; Nagar et al. 2001; Doi et al. 2005, 2011) compared to that expected by thermal synchrotron from RIAF ( $\alpha \gtrsim 0.4$ ; Mahadevan 1997). This may be reconciled by including nonthermal electron populations in RIAF (Yuan et al. 2003; Liu & Wu 2013) or considering convection processes (Narayan et al. 2000). Alternatively, as a simple analogy of more luminous AGN, such a discrepancy can be naturally accommodated if outflowing radio jets are

<sup>1</sup> We define spectral index as  $S_\nu \propto \nu^{+\alpha}$  in the present paper.

TABLE 1  
VLBA OBSERVATIONS OF M 104

UT Date	Frequency (GHz)	$\Delta\nu$ (MHz)	Beam size (mas $\times$ mas, deg.)	$I_p$ (mJy/bm)	$I_{rms}$ (mJy/bm)
		(a)	(b)	(c)	(d)
2008 Apr 26 <sup>†</sup> .....	1.430	32	$23.6 \times 5.70, -17$	51.8	0.068
2011 Mar 23.....	2.266	32	$9.44 \times 3.83, -4.2$	52.2	0.139
	4.990	64	$4.53 \times 1.95, 9.3$	67.6	0.091
	8.416	32	$2.42 \times 1.03, 1.1$	66.7	0.101
	15.36	64	$1.43 \times 0.54, -6.3$	72.9	0.215
	23.80	64	$0.97 \times 0.37, -8.7$	77.9	0.215
	43.21	64	$0.86 \times 0.23, -17$	82.2	0.51
2011 Mar 30.....	2.266	32	$9.75 \times 4.08, -6.8$	53.7	0.149
	4.990	64	$3.64 \times 1.55, -2.8$	64.8	0.088
	8.416	32	$2.47 \times 1.01, -3.3$	68.4	0.111
	15.36	64	$1.41 \times 0.54, -4.5$	77.5	0.167
	23.80	64	$1.01 \times 0.35, -8.4$	81.0	0.257
	43.21	64	$0.73 \times 0.24, -12.4$	87.9	1.03

Notes: <sup>†</sup> VLBA archival data (without Saint Croix, no phase-referencing mode); (a) total bandwidth; (b) synthesized beam with naturally-weighted scheme; (c) peak intensity of self-calibrated images of M 104 under naturally-weighting scheme (see Figure 1); (d) rms image noise level of M 104 images under naturally-weighting scheme.

present (Falcke & Biermann 1995, 1999, hereafter FB99)

Given their structural compactness and the radio regime being a key band, Very-Long-Baseline-Interferometry (VLBI) is a powerful tool to understand the nature of LLAGN activities. The nuclear structures are often unresolved even on milliarcsecond (mas) scale, constraining the size of radio emitting region to be  $\lesssim 10^{3-4}$  Schwarzschild radii ( $R_s$ ) with a brightness temperature of  $\gtrsim 10^{8-9}$  K (Ulvestad & Ho 2001). These unresolved cores show flat or only mildly inverted radio spectra, and their luminosities are generally too high to account for RIAF (Anderson et al. 2004). LLAGN with higher radio core luminosities tend to show elongated or extended structures on pc/sub-pc scale (Falcke et al. 2000; Nagar et al. 2002, 2005; Giroletti et al. 2005). Especially, in a couple of the best studied nearby cases such as M 81 and NGC 4258, the nuclear radio jets are evidently resolved together with an offset of the radio emitting site from their putative dynamical centers (Bietenholz et al. 2000, 2004; Herrnstein et al. 1997; Martí-Vidal et al. 2011), implying that significant amount of their accretion energy is channeled into outflowing jets (Markoff et al. 2008; Yuan et al. 2002; Doi et al. 2013).

Along with these sources, the nucleus of M 104 also represents an ideal case. A particularly striking advantage is its accessibility to the immediate vicinity of the central engine; due to its proximity and a large estimated black hole mass, their combination yields  $0.1 \text{ mas} = 0.004 \text{ pc} = 45.4 R_s$ . Such a physical scale in terms of  $R_s$  is  $\sim 5$  or  $\sim 20$  times finer than that of M 81 or NGC 4258, and even comparable to the accessible scales for the Galactic Center SgrA\* or the nearby radio galaxies M 87 and Cen A (Doi et al. 2009)<sup>2</sup>.

The M 104 nucleus has been intensively studied over the wide range of electromagnetic spectrum. At radio frequencies, the nucleus is completely pointlike on sub-arcsecond scale (de Bruyn et al. 1976; Krause et al. 2006). Non-simultaneous radio spectrum on arcsec scale is roughly flat with a typical flux density of  $\sim 100 \text{ mJy}$ , but vari-

abilities are reported on some of different amplitudes and time scales (de Bruyn et al. 1976; Hummel et al. 1984; Bajaja et al. 1988). Recent JCMT observations indicate the dominance of the AGN emission up to 350 GHz (Bendo et al. 2006). X-ray observations at 2-10 keV band show a point-like, hard ( $\Gamma = 1.89$ ) spectral shape nucleus with the absence of Fe K lines (Pellegrini et al. 2003). Bolometric luminosity of the nucleus is highly sub-Eddington ( $L_{bol} \sim 2.5 \times 10^{41} \text{ erg s}^{-1} \sim 2 \times 10^{-6} L_{Edd}$ ; Pellegrini et al. 2003), and the overall characteristics of its broadband SED is similar to those of other LLAGN (Ho 1999).

Despite such observational advantages, little is known yet about its milliarcsecond-scale structure. Early VLBI experiments of this nucleus shows a single unresolved component ( $< 2.7 \text{ mas}$ ) without any signs of extended feature (Graham et al. 1981; Preston et al. 1985; Shaffer & Marscher 1979). More recently, a few of snap-shot images are obtained from geodetic RDV<sup>3</sup> observations at 2 and 8 GHz, but the nucleus still looks point like. However, the sensitivities and the resolutions of these observations are relatively poor; to uncover the exact nature of its nuclear structure, more dedicated observations are indispensable. Indeed, some of theoretical studies predict a structural complexity for the nuclear structure of M 104 (Di Matteo et al. 2001; Yuan et al. 2009).

In this paper, we report on our deep VLBI observations toward the nucleus of M 104. Thanks to the use of quasi-simultaneous, multi-frequency, phase-referencing mode at a higher sensitivity, we have obtained a number of new findings on the nuclear structure of this source. The data and the analysis are described in the next section. We show the results in section 3, and then discuss the physical properties of the M 104 nucleus in section 4. Finally, we summarize our main conclusions in section 5.

## 2. OBSERVATIONS AND DATA REDUCTION

On 23 and 30 March 2011, we observed the M 104 nucleus with VLBA at 2.3, 5.0, 8.4, 15.4, 23.8 and 43.2 GHz quasi-simultaneously. The observations involved rapid switching

<sup>2</sup> In terms of the black hole mass of Cen A, Doi et al. (2009) assume  $\sim 2 \times 10^8 M_\odot$  (Marconi et al. 2001). However, more recent measurements revise its mass toward a smaller value  $\sim 5 \times 10^7 M_\odot$  (see Neumayer 2010, and references therein). In this case, M 104 has a larger apparent diameter of the central black hole than that of Cen A.

<sup>3</sup> Research and Development with the Very-Long-Baseline-Array (VLBA); e.g., Gordon (2005).

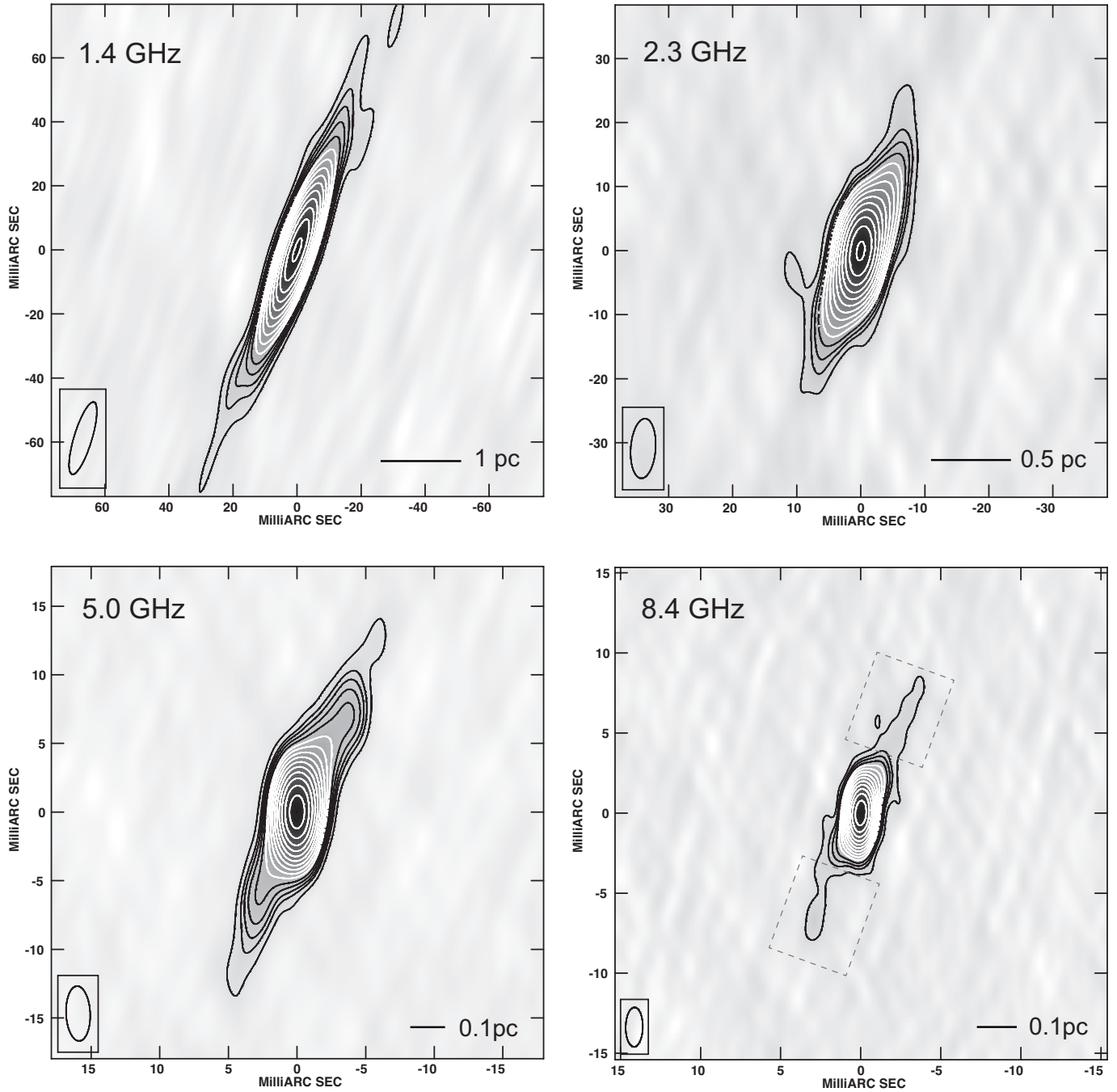


FIG. 1.— VLBA images of the M 104 nucleus at all the observed frequencies. Naturally-weighted scheme is used for each data and the synthesized beam are shown in bottom-left corner of each image. Contours start from  $-1, 1, 2, \dots$  times  $3\sigma$  image rms level and increasing by factors of  $2^{1/2}$ . The length of the horizontal bar in bottom-right corner of each image indicates a linear scale of each image on pc unit. Two rectangular areas enclosed by dashed lines on 8.4 GHz image ( $6 \times 5 \text{ mas}^2$  in  $P.A. = -20^\circ$  or  $P.A. = 160^\circ$  starting from 4 mas distance from the core peak for each rectangle) indicate the regions where the brightness ratio of the northern/southern extended components are measured by integrating the CLEAN components (adopted rectangular regions at each frequency are summarized in Table 2).

between M 104 and the nearby radio source J1239–1023, which is separated by  $1.23$  on the sky, plus a few scans of the bright fringe-finder source 3C 279. To reduce systematic errors and to achieve nearly the same  $uv$  coverage among frequencies, we carried out observations by alternating each frequency in turn every 10–40 minutes. Each session was conducted in a 10-hour overnight run at a data recording speed of 512 Mega-bit per second. All of the 10 VLBA stations were participated.

The initial data calibration was performed using the Na-

tional Radio Astronomy Observatory (NRAO) Astronomical Image Processing System (AIPS) based on the standard VLBI data reduction procedures. The amplitude calibration with opacity corrections was applied using the measured system noise temperature and the elevation-gain curve of each antenna. We next performed apriori corrections for the visibility phases; antenna parallactic angle differences between M 104 and J1239–1023, ionospheric dispersive delays using the ionospheric model provided by the Jet Propulsion Laboratory (JPL), and instrumental delays/phases using a scan

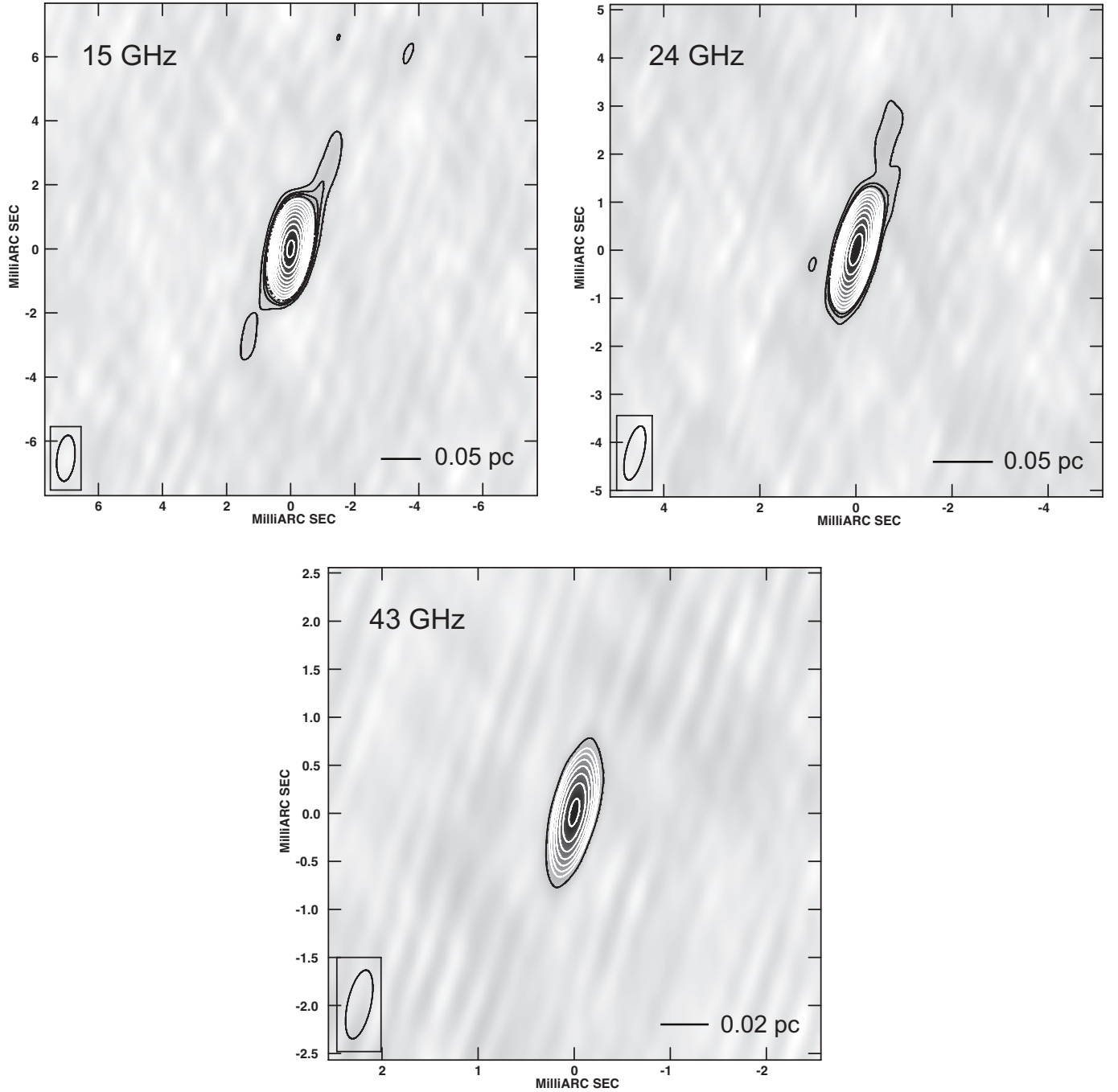


FIG. 1.— Continued.

of 3C 279 were corrected. Then, to create images of M 104 and J1239–1029, we performed a fringe-fitting on each source separately and removed residual delays, rates and phases assuming a point source model. We clearly detected fringes for these data with sufficient signal-to-noise ratios ( $\text{SNR} > 7$ ) except for M 104 at 43 GHz, where the fringe-fitting failed for many of the scans due to insufficient SNR. As described below, however, we successfully recovered the solutions for these scans by referencing the phase/gain solutions derived by J1239–1023 (a few to several hundreds of mJy so bright enough to detect fringes). Images were created in DIFMAP software (Shepherd 1997) with iterative phase/amplitude self-calibration. Because M 104 is not so bright, amplitude self-

calibration for this source was performed with relatively long solution intervals (60 ~ 300 minutes, depending on SNR of each data).

In terms of astrometric investigations for M 104, we performed the phase-referencing analysis in the following way. After the apriori corrections of the parallactic angle, ionosphere and instrumental delays, we performed a fringe-fitting only on J1239–1023 with its source model created by the previous imaging process at each frequency (see Appendix for the detailed structure this source). With this process, we derived the solutions for residual phases/delays/rates, in which the effect of the source structure is already considered. These solutions were then transferred to the time segments of M 104.

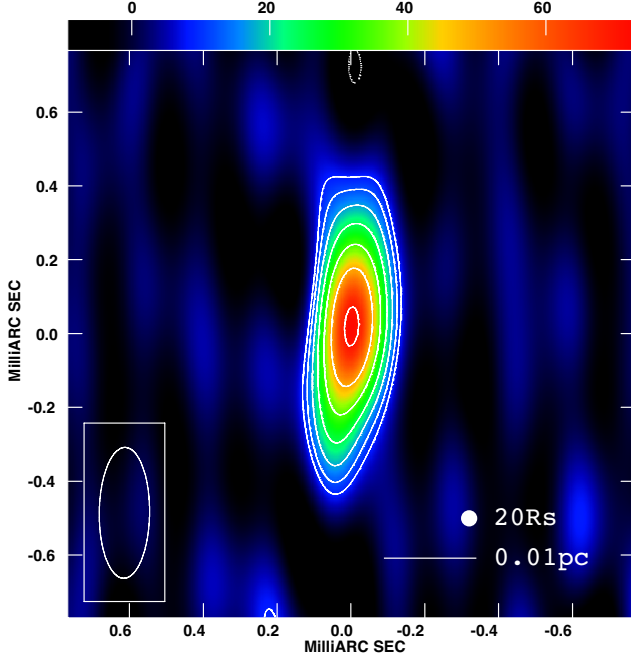


FIG. 2.— The highest resolution image of the M 104 nucleus at 43 GHz with uniform weighting scheme. The synthesized beam is  $0.354 \text{ mas} \times 0.136 \text{ mas}$  at P.A. =  $-1^\circ$  (shown in bottom-left corner of each image). Contours start from  $-1, 1, 2, \dots$  times  $6 \text{ mJy beam}^{-1}$  ( $3\sigma$  image rms) and increasing by factors of  $2^{1/2}$ . The peak flux density is  $73 \text{ mJy beam}^{-1}$ . Physical scales in parsec and  $R_s$  units are indicated in the bottom-right corner of the image.

After that, we ran the AIPS task CALIB on J1239–1023 (with the source model) to derive the corrections of the time-dependent gains for each antenna. Finally, these gain corrections were transferred to the scans of M 104. Through these processes, we successfully obtained the phase-referenced images of M 104, in which the relative position of M 104 with respect to J1239–1023 is conserved. The astrometry results are shown in section 3.4.

Additionally, we found one VLBA archival data of M 104 at 1.4 GHz, which was observed for a relatively long integration time ( $\sim 2.5$  hours) with 9 stations (no Saint Croix). Although this data set is not obtained with astrometry mode and the epoch is more than 2 years separated from our observations, this is still useful to understand the nuclear structure at lower frequency side. We then include this data in the present study and analyzed based on the standard data reduction process.

### 3. RESULTS

#### 3.1. Images

In Figure 1, we show self-calibrated images of the M 104 nucleus at all the observed frequencies. Between 2 and 43 GHz, the images shown are made by stacking the visibility data over the two epochs. We did not find any significant structural/flux variations at each frequency over the two epochs within the calibration uncertainties.

Thanks to high qualities of the data set, we have obtained VLBI images for the M 104 nucleus at unprecedented sensitivities and resolutions. To our knowledge, this is the first clear VLBI detections and imaging of M 104 at 15, 24 and 43 GHz. In particular at 43 GHz, where the angular resolution attains  $0.35 \times 0.14 \text{ mas}$  with uniform weighting scheme, the nuclear structure was imaged on a scale down to  $\sim 60 R_s$  (Figure 2). Along with SgrA\* (Shen et al. 2005; Doeleman et al. 2008; Lu et al. 2011), M 87 (Junor et al.

TABLE 2  
M 104 NORTHERN/SOUTHERN BRIGHTNESS RATIO

Frequency (GHz)	Box in P.A. = $-20^\circ$ and $160^\circ$ (radial range from core in mas)	$S_N$ (mJy)	$S_S$ (mJy)	$R$
	(a)	(b)	(c)	(d)
1.430	30 – 50	1.2	1.1	1.1
2.266	10 – 30	2.3	2.1	1.1
4.990	6 – 14	2.7	2.2	1.2
8.416	4 – 10	1.8	1.4	1.3
15.36	2 – 7	2.3	1.4	1.6
23.80	1.5 – 3.5	2.0	0.96	2.1

Notes: (a) box region in which the CLEAN components were integrated (see Figure 1 for the case at 8.4 GHz); (b) integrated CELAN flux in the northern box; (c) integrated CELAN flux in the southern box; (d) brightness ratio defined as  $S_N/S_S$ . We used source structure models of M 104 which were created by stacking the two epochs.

TABLE 3  
GEOMETRICAL PARAMETERS OF THE MODELFITTED CORE

Frequency (GHz)	$\theta_{\text{maj}}$ (mas)	$\theta_{\text{min}}/\theta_{\text{maj}}$	P.A. (deg.)
	(a)	(b)	(c)
1.430	$11.4 \pm 5.1$	0.09	$-24 \pm 5$
2.266	$5.22 \pm 1.8$	0.16	$-24 \pm 5$
4.990	$1.55 \pm 0.49$	0.25	$-25 \pm 5$
8.416	$0.75 \pm 0.29$	0.06	$-29 \pm 5$
15.36	$0.37 \pm 0.12$	0.34	$-31 \pm 5$
23.80	$0.26 \pm 0.08$	0.19	$-30 \pm 5$
43.21	$0.22 \pm 0.08$	0.21	$-14 \pm 10$

Notes: (a) major axis sizes of the derived elliptical Gaussians; (b) axial ratios of the derived Gaussian models; (c) position angles of the major axes of the Gaussian models.

1999; Krichbaum et al. 2006; Ly et al. 2007; Hada et al. 2011; Doeleman et al. 2012) and Cen A (Tingay et al. 1998; Horiuchi et al. 2006; Müller et al. 2011), M 104 is the fourth source in which such a compact scale was resolved. The obtained image parameters for these maps are listed in Table 1.

In the previous radio observations, only a single compact feature was detected for the nuclear region both on arcsec (de Bruyn et al. 1976; Hummel et al. 1984; Bajaja et al. 1988; Krause et al. 2006) and mas scales (Graham et al. 1981; Preston et al. 1985; Shaffer & Marscher 1979). In the new experiments presented here, for the first time, we have clearly discovered the presence of the extended structure elongating from the radio core. This structure is more remarkable at lower frequencies, and appears to elongate quite symmetrically toward a northwest (P.A.  $\sim -20^\circ$ ) and a southeast (P.A.  $\sim 160^\circ$ ) directions. Its entire length is estimated to be  $\sim 120 \text{ mas}$  ( $4.8 \text{ pc}$  or  $5.4 \times 10^4 R_s$ ) at 1.4 and  $\sim 30 \text{ mas}$  ( $1.2 \text{ pc}$  or  $2.7 \times 10^5 R_s$ ) at 5 GHz (above  $3\sigma$  level), respectively. Note that the direction of the extension is similar to that of the major axis of synthesized beams, but we are confident that this structure is not an artifact; the extension of this structure is sufficiently larger than each beam size, and a consistent structure is obtained also at 5 GHz, where the position angle of the synthesized beam is significantly different from that of the source elongation. The extended structure is quite smooth and none of knotty features was found.

As frequency increases, the structure becomes progressively compact, and the radio core increasingly dominates the total radio emission. At 15 and 24 GHz, the northern



TABLE 4  
M 104 SPECTRA FOR SEVERAL REGIONS

Regions	$S_{1.4}$ (mJy)	$S_{2.3}$ (mJy)	$S_{5.0}$ (mJy)	$S_{8.4}$ (mJy)	$S_{15.2}$ (mJy)	$S_{23.8}$ (mJy)	$S_{43.2}$ (mJy)	$\alpha_{ave}$
(1) Total	$67.3 \pm 6.7$	$76.1 \pm 7.6$	$90.8 \pm 9.1$	$91.0 \pm 9.1$	$95.4 \pm 9.5$	$92.6 \pm 9.3$	$91.2 \pm 9.1$	0.08
(2) Core	$59.6 \pm 6.0$	$62.1 \pm 6.2$	$74.3 \pm 7.4$	$80.2 \pm 8.0$	$87.1 \pm 8.7$	$88.0 \pm 8.8$	$91.0 \pm 9.1$	0.14
(3) Extended	—	$31.9 \pm 6.4$	$15.2 \pm 3.0$	$8.3 \pm 1.7$	$3.8 \pm 0.8$	$2.5 \pm 0.5$	$< 1.5$	-1.10

Notes: see the text for the definition of each region (1), (2) and (3). Because of its large beam size (23 mas), reliable measurement of  $S_{1.4}$  for the outside of 4-mas-diameter circle was not possible (severe blending between the core and the outer emission).

side emission tends to be brighter than that of the southern one. We then estimated a brightness ratio  $R$  of the northern/southern emission at each frequency in the following way; using the source structure model established by deconvolution process (i.e., a set of CLEAN components), we compared integrated flux densities of CLEAN components in two rectangular regions, which are at the same distance from the core having the same size (one is along P.A. =  $-20^\circ$  and the other is along P.A. =  $160^\circ$ ). The results are summarized in Table 2.  $R$  were derived to be  $\sim 1.1$ – $1.2$  between 1.4 and 5 GHz, whereas  $\sim 1.3$ – $2.1$  between 8.4 and 24 GHz. Note that derived value of  $R$  at each frequency varied slightly when we changed the shape of the adopted box, but the overall trend was basically the same as the case in Table 2 and the northern side was brighter. At 43 GHz, almost all of the emission above  $3\sigma$  is confined within  $\sim 1$  mas.

### 3.2. Modelfitting

To quantify the structural properties of the M 104 nucleus, we performed a modelfitting to the images. As a simple description, here we performed a single elliptical Gaussian modelfitting to the core region using the AIPS task JMFIT, and derived deconvolved parameters of the models. Note that the actual structure is more complicated as evident from the pres-

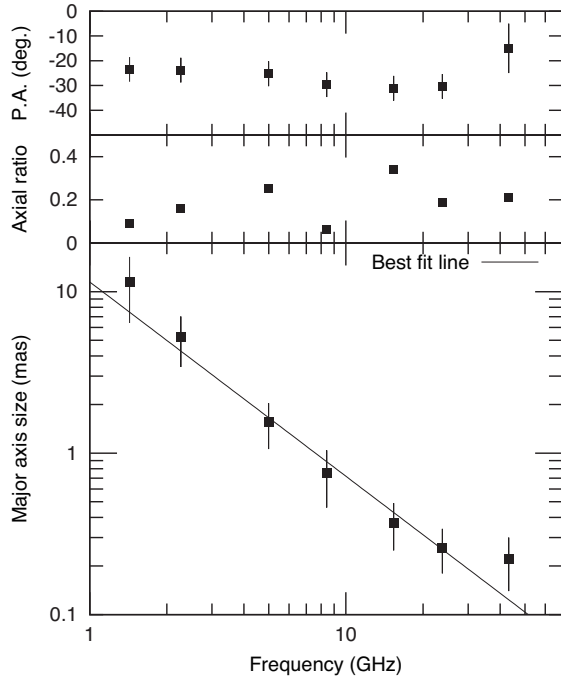


FIG. 3.— Radio core parameters of the M 104 nucleus as a function of frequency. (Top) position angles of major axis of the derived elliptical Gaussians. (Mid) axial ratios of the derived Gaussian models. (Bottom) major axis size of the radio core. The solid line indicates the best-fit solution of the frequency dependence of the major axis size  $\theta_{maj} \propto \nu^{-1.20 \pm 0.08}$ .

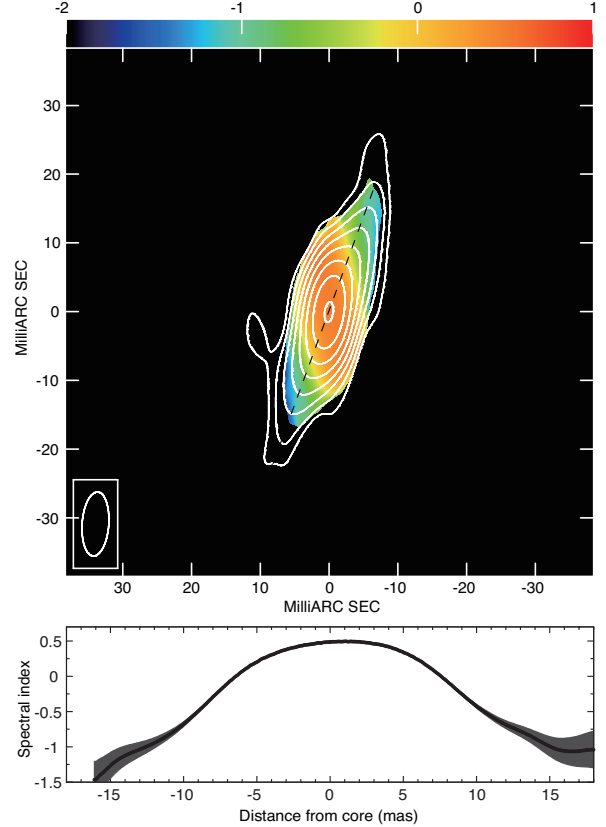


FIG. 4.— Spectral index distribution map between 2.3 and 5.0 GHz and its slice along P.A. =  $-20^\circ$ . The color scale indicates values of spectral index  $\alpha$ , while the overlaid contours indicates the intensity image at 2.3 GHz. Both of images were commonly convolved with the naturally-weighted 2.3 GHz beam (shown in the bottom-left corner of the map). The spectral indices were then calculated in the region where the flux densities are above  $5\sigma$  image noise level both at 2.3 and 5.0 GHz. The contours starts from 1, 2, 4... times  $0.4 \text{ mJy beam}^{-1}$  and increasing by factors of 2. In the slice plot, the positive direction of horizontal axis corresponds to the northern direction. The gray area in the slice plot indicates an uncertainty of the spectral index at each distance, which is estimated using  $1\sigma$  noise level of each image.

ence of the extended emission, but this method is still useful to examine the basic properties of the main emitting component (i.e., radio core). The obtained values for the geometrical parameters are summarized in Table 3 and shown in Figure 3 as a function of frequency.

At all the observed frequencies, the derived Gaussian models show highly elongated shapes in a mean position angle of P.A.  $\sim -25^\circ$  (or  $155^\circ$ ), which smoothly connects to the direction of the larger scale extension. In terms of the core size, the length of the major axis ( $\theta_{maj}$ ) is clearly frequency dependent, becoming smaller as frequency increases. We examined an averaged frequency dependence of the major axis size by fitting a power-law function to the data between 1.4 and 43 GHz, and obtained the best-fit solution as

$\theta_{\text{maj}} \propto \nu^{-1.20 \pm 0.08}$ . On the other hand, the structure along the minor axis tends to be largely unresolved; the derived lengths result in typically  $\sim 1/5$  of the beam size or smaller at each frequency. At 43 GHz, the size of the radio core is derived as  $0.22 \text{ (mas)} \times 0.08 \text{ (mas)}$  in P.A. =  $-20^\circ$  with a flux density of 91 mJy, corresponding to  $0.009 \times 0.003 \text{ pc}$  ( $1900 \times 600 \text{ AU}$ ) or  $100 \times 36 R_s$ . With this parameter set at 43 GHz, the brightness temperature of the most compact region is estimated to be  $\sim 3 \times 10^9 \text{ K}$ . If the obtained size of the minor axis is treated as an upper limit, this brightness temperature would be regarded as a lower limit.

We note that a frequency-dependent size of the radio core is also seen in the M 81 nucleus with a slightly shallower profile ( $\propto \nu^{-0.8}$ ; Bietenholz et al. 1996, 2004; Ros & Pérez-Torres 2012). We also remark that no signs of the scatter-broadening law, which is obviously seen toward SgrA\* as  $\theta \propto \nu^{-2}$  (Lo et al. 1993), was found in the case of M 104, despite that a comparable physical scale is observed in gravitational unit.

### 3.3. Spectra

Multi-frequency images of M 104 shows the nuclear radio structure to be clearly frequency dependent, indicating that the spectral property is spatially varying. We then investigated the spectral properties and their spatial distributions. Quasi-simultaneous observations with a wide frequency coverage at good image qualities allow us to examine these in detail.

In Figure 4, we firstly show a spectral index distribution map between 2 and 5 GHz and its slice along P.A. =  $-20^\circ$  in order to qualitatively describe an overall spectral characteristics. The two images at 2 and 5 GHz are aligned by the respective phase centers. While a careful alignment is

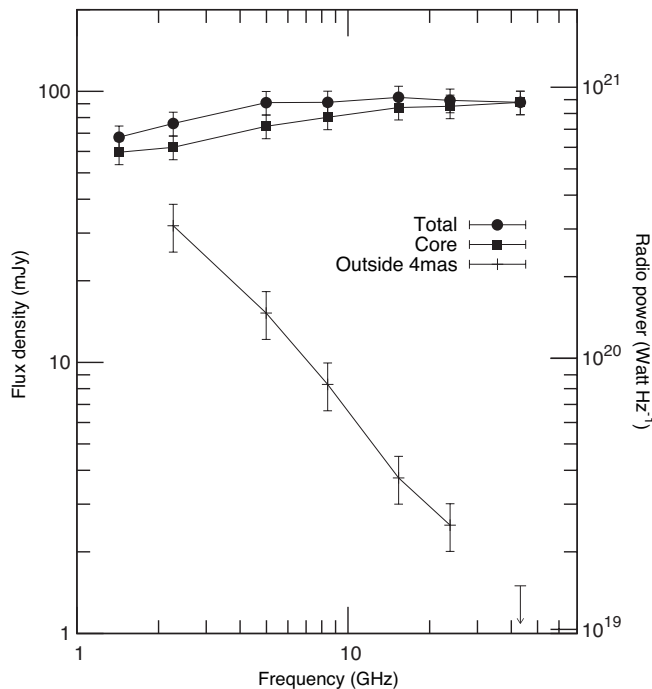


FIG. 5.— VLBA radio spectra of the M 104 nucleus. The spectra for three different regions are plotted: (1) entire CLEANed VLBI flux, (2) radio core flux derived by modelfitting in the previous section, (3) integrated CLEANed flux of the extended region. For (3), we defined the region as the outside of a 4-mas-diameter circle centered on the core. For the extended region at 43 GHz, we calculated an upper limit based on the image rms level.

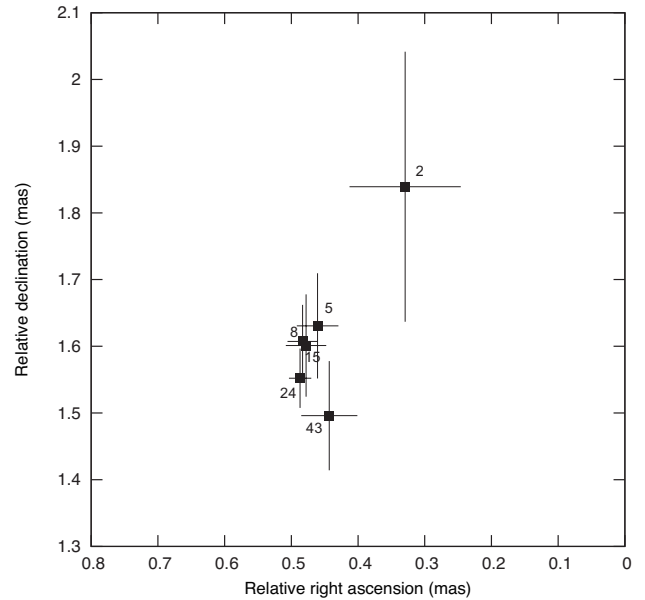


FIG. 6.— Astrometry of the M 104 core position at each frequency with respect to the centroid of an optically-thin feature in J1239–1023. The weighted mean position over the two epochs are plotted at each frequency. The number close to each data point indicates the observed frequency for each data. The quoted position error at each frequency refers to the statistical error budget, which is calculated by root-sum-squaring the position uncertainties of the M 104 core (phase-referenced image) and the reference feature in J1239–1023 (self-calibrated image). As the coordinate origin of this plot, the nominal phase-tracking center for M 104 R.A. =  $12^{\text{h}}39^{\text{m}}59^{\text{s}}.4318650$ , decl. =  $-11^\circ37'22''.996380$  (J2000) are used.

necessary if one seeks for a more accurate distribution, the frequency-dependent position shift of the radio core between these frequencies are small compared with the structural extension (see the next section). Thus Figure 4 gives a reasonable approximation for the true spectral distribution. As seen in this map, the M 104 nucleus clearly shows a spatially-varying spectral property. The spatial gradient of the spectral index distribution is apparent along the source elongation; the spectrum is slightly inverted near the core and progressively become steep as receding from the core towards both the northern and southern directions.

Then, we combined all of the multi-frequency data to clarify more detailed spectral properties. In Figure 5 and Table 4, we show combined radio spectra between 1.4 and 43 GHz. Here we plot the spectra for three different regions: (1) the total CLEANed VLBI flux, (2) the radio core flux derived by the modelfitting in the previous section, (3) the integrated CLEANed flux for the extended region. For (3), we defined such a region as the outside of 4-mas-diameter circle centered on the core, which corresponds to the exterior part of the modelfitted core at  $>2 \text{ GHz}$ . We stress that these spectra are quasi-simultaneously obtained between 2 and 43 GHz, which is essential to correctly understand the spectral properties.

Over the observed frequency range, the total emission shows a quite flat spectrum with an averaged spectral index of  $\alpha = 0.08 \pm 0.03$ . However, our high-resolution observations revealed that such a total spectrum consists of distinct spectral components. The radio core shows an slightly inverted spectrum with an averaged spectral index  $\alpha = 0.14 \pm 0.02$ , whereas the extended part shows a steep spectrum with  $\alpha = -1.11 \pm 0.04$ .

### 3.4. Astrometry of the core

One of the key approaches to specify the origin of nuclear radio emission is to examine the position shift of the radio core as a function of frequency. This “core shift” is expected as a natural consequence of the nuclear opacity effect if the radio emitting region is dominated by a radio jet (Königl 1981; Lobanov 1998; Falcke & Biermann 1999; Hada et al. 2011). Our quasi-simultaneous, multi-frequency, phase-referencing observations relative to the calibrator J1239–1023 allow us to examine this.

In Figure 6, we show the astrometry results of the M 104 core positions. Here we plot an weighted mean position over the two epochs at each frequency to better constrain the position. While the jet base structure of J1239–1023 is relatively complex, we detected a well-isolated, bright optically-thin feature A1 in the downstream side of this jet (see Appendix on the structure of J1239–1023). So we measured the relative position of the M 104 core at each frequency with respect to the intensity centroid of this feature, which is supposed to be stationary on the sky in terms of frequency (Kovalev et al. 2008; Sokolovsky et al. 2011). For both of the M 104 core and the reference feature in J1239–1023, their positions were registered using a Gaussian model fitting on each image. The quoted position uncertainties in Figure 6 refer to statistical terms, which are purely caused by image qualities (phase-referenced images for M 104 core whereas self-calibrated images for the reference feature in J1239–1023), by calculating the beamsize divided by the peak-to-noise ratio of each component.

The derived result indicates that the observed core positions tend to move toward a northern direction as frequency decreases, although the position uncertainties are rather large because M 104 is a low-declination source. An overall position angle of the shift is roughly  $-10^\circ \sim -30^\circ$ , which is similar to the direction of the larger-scale northern extension. Mean values of the observed position shifts are measured to be  $\sim 0.2$  mas,  $\sim 0.3$  mas and  $\sim 0.4$  mas for 2–5 GHz, 2–24 GHz and 2–43 GHz pairs, respectively.

We should note that, while non-dispersive tropospheric residuals produce a common systematic position shift at different frequencies (thus such shifts can be canceled out among frequencies in our quasi-simultaneous observations), dispersive ionospheric residuals can cause an unwanted frequency-dependent position shift. We then checked a possible impact of the ionospheric effect by comparing the astrometry results made with and without the ionospheric correction (AIPS task TECOR). Phase-referenced images without the correction produced position shifts of M 104 as large as  $\sim 3$  mas toward a similar (P.A.  $\sim 0^\circ$ ) northern direction between 2 and 43 GHz with degrades of image qualities ( $\sim 30\%$  decrease of the peak-to-noise ratio was seen at 2 GHz). So one cannot completely exclude the possibility that the observed northward shifts are related to the ionospheric effect. However, we confirmed that the amount of position differences between the two methods was well fitted by an inverse-square law with frequency  $\nu^{-2.19 \pm 0.20}$ , indicating that the ionospheric correction is indeed working effectively. Using the equation provided in Hada et al. (2011), we estimate a potential remaining uncertainty due to the ionospheric residuals after the correction to be  $\sim 0.2$  mas at 2 GHz, under the observed condition of  $\delta Z = 1.23$ ,  $Z \sim 50^\circ$  and  $\delta I \sim 3 \times 10^{16} \text{ m}^{-2}$  where  $\delta Z$ ,  $Z$  and  $\delta I$  represent the source separation, source zenith angle and residual total electron content, respectively. Hence, if the position measurements are still affected by the ionospheric residuals,

the observed  $\sim 0.2$  mas shift for 2–5 GHz pair would be regarded as an upper limit, and for the pair of 2–24 GHz or 2–43 GHz, a level of  $\sim 0.1$ – $0.2$  mas is eventually left for the intrinsic core shift.

### 3.5. Variability

Previous arcsec-scale observations report that the M 104 nucleus is variable at radio frequencies at some of different time scales and amplitudes. de Bruyn et al. (1976) report a  $10\sim 20\%$  level variability at 5 and 8 GHz during a period of a few months, whereas Bajaja et al. (1988) found a  $\sim 70\%$  level flux increase at 1.7 GHz between 1971 and 1986. We searched for any possible variability by comparing the data on March 23 and 30 separately. However, no significant variability was found for any component within the amplitude calibration accuracy ( $\sim 10\%$ ).

The observed VLBI flux densities of  $\lesssim 100$  mJy are  $20\sim 40\%$  lower than those measured in previous VLBI experiments at 2 and 5 GHz ( $\sim 120$ – $140$  mJy) (Graham et al. 1981; Shaffer & Marscher 1979). This implies the presence of a long-term variability on mas scale.

## 4. DISCUSSION

Probing the nucleus of M 104 provides clues to understand the physical processes acting in the vicinity of a very sub-Eddington black hole. Here we discuss the nuclear structure of M 104 based on the new high-resolution radio results as well as information at other bands.

### 4.1. Evidence for nuclear radio jet

Because of its highly sub-Eddington luminosity and the absence of Fe K $\alpha$  lines, it is suggested that the standard thin accretion disk is not present in the nuclear accretion of M 104 (Pellegrini et al. 2003). Similarly to other LLAGN, its accretion state is preferably modeled by RIAF (Di Matteo et al. 2001; Yuan et al. 2009). However, a predicted amount of RIAF emission with its Bondi-accretion rate ( $\dot{M}_{\text{Bondi}}$ ) overestimates the observed radio luminosity by a factor of  $\sim 10$  (Di Matteo et al. 2001); to reconcile the RIAF model, they point out the necessity of reducing the accretion rate down to a few percent of  $\dot{M}_{\text{Bondi}}$  near the inner edge of the accretion flow. Such an inward decrease of the accretion rate can be realized via outflow/winds (adiabatic inflow-outflow solution (ADIOS); Blandford & Begelman. 1999) or convection (convection-dominated accretion flow (CDAF); Narayan et al. 2000), although recent studies tend to disfavor the latter scenario because the real accretion flow is convectively stable (Yuan et al. 2012; Narayan et al. 2012). On the other hand, RIAF with such a strong mass loss leads to a significant reduction of the radio-to-X-ray luminosity ratio ( $L_{\text{radio}}/L_X$ ) from the original (non-mass loss) RIAF (Quataert & Narayan 1999). This situation then leads to a significant “underestimate” of the expected radio emission once the model attempts to match the observed X-ray luminosity. In the end, these theoretical studies come to conclude that the presence/dominance of a nuclear radio jet is a natural solution in order to consistently explain the observed luminosities at radio/X-ray, and the requirement of mass loss (Di Matteo et al. 2001; Yuan et al. 2009). Nonetheless, previous radio observations of M 104 have not found such a jet like signature so far; only a point-like structure was seen both on arcsec (de Bruyn et al. 1976; Hummel et al. 1984; Bajaja et al. 1988; Krause et al. 2006) and mas (Graham et al.



1981; Preston et al. 1985; Shaffer & Marscher 1979) scales, resulting in a major puzzle for the nuclear structure of M 104.

In this work, our deep VLBA observations have finally obtained compelling evidence for the nuclear radio jets in the center of M 104. In terms of its morphology, the pc to sub-pc scale structure is never point-like, but clearly has an extended component. This extended structure is narrow and collimated with a two-sided shape, and both sides show steep radio spectra at the observed frequency range. At the base of the extended structure, the central radio core shows a high brightness temperature with a flat~slightly inverted spectrum. The model fitting shows the radio core to be highly elongated in the same direction of the outer extended structure with a clear frequency-dependent size. Moreover, the astrometric measurement shows a tendency of the core position shift with frequency. While these characteristics cannot be explained by thermal synchrotron from RIAF, all of the observed radio properties share the well-known characteristics in more luminous AGN such as FR I or FR II radio galaxies; the radio emission is created by nonthermal synchrotron emission from relativistic jets with spatially-varying nuclear opacities. Note that creating higher brightness temperatures and flatter spectra of radio core are still possible with RIAF itself if one introduces a nonthermal electron population in the accretion flow (Yuan et al. 2003; Liu & Wu 2013). However, such a RIAF-dominated scenario would have still difficulty in explaining the observed geometrical properties of the radio core; the emission region of such a hot accretion flow is nearly spherically symmetric (Narayan & Yi. 1994), thus does not expect a significant elongation of the emitting region and a core shift toward a specific direction. Based on a number of these new evidence, therefore, we argue that the radio emission of the M 104 nucleus is dominated by the nuclear radio jets emanating from its central engine over the observed frequencies.

It should be noted that the nuclear radio jets are similarly resolved in the other nearest cases M 81 (3.6 Mpc) and NGC 4258 (7.2 Mpc) together with an obvious offset of the radio cores from their putative black hole positions (Bietenholz et al. 2000, 2004; Herrnstein et al. 1997; Doi et al. 2013). Since the radio powers of these sources ( $P_{5G} \sim 10^{20.9}, 10^{20.4}$  and  $10^{19.3}$  W Hz<sup>-1</sup> for M 104, M 81 and NGC 4258) fall on a roughly intermediate level among LLAGN population (Nagar et al. 2005), this implies that the production of jets is a common ability of LLAGN central engines. Regarding more distant sources, Ulvestad & Ho (2001) and Anderson et al. (2004) have shown in six prototypical LLAGN (at distances between 15~40 Mpc with their radio powers ranging  $P_{5G} \sim 10^{19.5-21}$  W Hz<sup>-1</sup>, comparable to those of the above three sources) that their nuclear radio structures are unresolved on mas scale, but too bright to be explained by RIAF. This situation would be naturally expected if their jets are highly compact similarly to those seen in M 104, M 81 and NGC 4258. We also note that recent high-sensitivity VLBI studies suggest the dominance of jet emission in some of the faintest end of LLAGN (down to around  $10^{19}$  W Hz<sup>-1</sup>; Giroletti & Panessa 2009; Bontempi et al. 2012).

#### 4.2. Physical properties of the M 104 jet

We attempt to estimate fundamental parameters of the M 104 jet based on the obtained radio results.

First, since the M 104 nucleus shows a two-sided structure, it is important to determine which is the approaching jet and

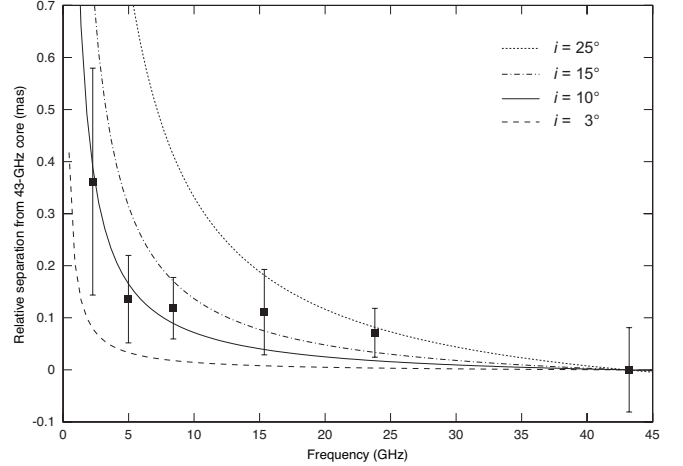


FIG. 7.— Comparisons of the observed core shift with the compact jet model in FB99 for different inclination angles. We plot the observed core separation relative to the 43-GHz core position at each frequency. The quoted position uncertainty at each frequency is calculated by root-sum-squaring the position errors in  $x$  and  $y$  directions used in Figure 6. In the calculations of the FB99 model, we adopt a black hole mass  $1.0 \times 10^9 M_{\odot}$ , a distance  $d = 9.0$  Mpc, a characteristic electron Lorentz factor  $\gamma_e = 300$ , and a mean radio core flux density 77 mJy over the observed frequencies. The cases of four different inclination angles  $i = 3^{\circ}$  (long-dash line),  $i = 10^{\circ}$  (solid line),  $i = 15^{\circ}$  (dot-dash line) and  $i = 25^{\circ}$  (dot line) are plotted.

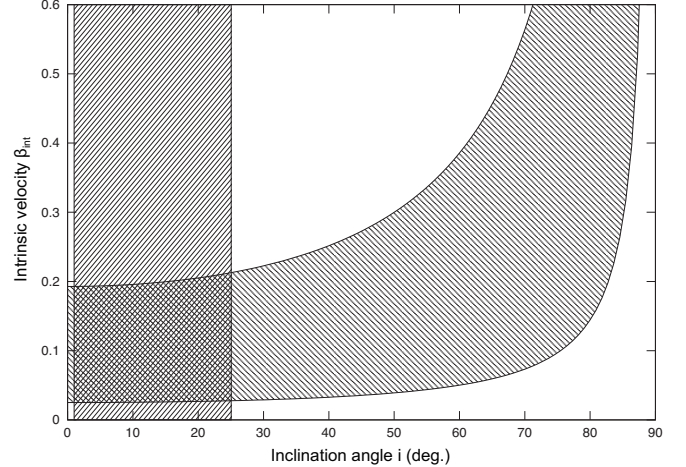


FIG. 8.—  $(\beta_{\text{int}} - i)$  plane for the M 104 jet. The shaded area enclosed by the two curved lines indicates the allowed parameter space estimated by the brightness ratio between  $R = 1.1$  and  $R = 2.1$ . The shaded area enclosed by the two vertical lines indicates the range of inclination angle constrained by the comparison of the observed core shift with the compact jet model by FB99 (see Figure 7). The overlapped area of the two regions (in the bottom-left corner of the plane) indicates the allowed parameter space for the M 104 jet.

the other side is receding. Assuming that the two-sided jet is intrinsically symmetric and any of apparent asymmetry is caused by Doppler-beaming/de-beaming effects, here we claim that the northern part is the approaching jet. This is because, while the observed structures at 1.4 and 2.3 GHz are relatively symmetric, at higher frequencies the northern part tends to become brighter than the southern part with a brightness ratio  $R = 1.3 \sim 2.1$ . This argument is also supported by a tendency of the core shift toward the northern direction as frequency decreases.

Next, by using the brightness ratio of the jet/counter-jet, we estimate an allowed range of the inclination angle  $i$  and the intrinsic velocity  $\beta_{\text{int}} = v_{\text{int}}/c$ . In general, these two parameters are derived simultaneously by measuring a brightness ra-

tio and an apparent jet velocity. However, the data used here are not enough to measure the jet motion reliably. Instead, here we attempt to constrain  $i$  by comparing the observed core shift with a theoretical expectation assuming that the observed radio core at each frequency marks a synchrotron-self-absorption surface of the approaching jet.

According to the compact jet model proposed by FB99, the amount of the core shift in LLAGN jets is mainly dependent on observing frequency, characteristic electron Lorentz factor  $\gamma_e$ , and inclination angle of the jet. This model has been applied to several LLAGN such as SgrA\*, M 81, NGC 4258 as well as some of galactic sources, and successfully explain many observational aspects of these sources. In Figure 7, we show a comparison of the observed core shift (relative to the 43 GHz core position) with model predictions for several different inclination angles. We calculated these expected values by combining the equations (8) and (16) in FB99 under the assumption of  $\gamma_e = 300$ , which is suggested to be a typical value for LLAGN (similar discussion is presented in Anderson et al. 2004).

Because the observed core shift is relatively small, matched models suggest small inclination angles around  $i \sim 3\text{--}15^\circ$ . For larger  $i$ , e.g.,  $i = 25^\circ$ , the model still matches the observed core shift between 43 GHz and 15/24 GHz within the uncertainties, but tends to overestimates the values at lower frequencies. We also checked the impact of  $\gamma_e$  by changing its value between 250 and 630, the range of which is implied by the modeling of M 81 and NGC 4258 (FB99). We confirmed that this uncertainty of  $\gamma_e$  eases the allowed range of  $i$  to be about  $1^\circ\text{--}25^\circ$  in order to reproduce  $0.1\text{--}0.7$  mas separation between 2 and 43 GHz. In fact, this range of  $i$  creates integrated jet luminosities with flat  $\sim$  only mildly inverted radio spectra  $\alpha \sim 0\text{--}0.10$  in their model ( $S_\nu \propto \nu^{0.20\pm 0.02}$  where  $\xi_2 \equiv -0.155 + 1.79i - 0.634i^2$ ; equation (8) in FB99), which is consistent with the observed integrated spectrum for M 104 ( $\alpha \sim 0.08 \pm 0.03$ ). Thus, a range of  $1^\circ < i < 25^\circ$  would be a reasonable constraint on the inclination angle of the M 104 jet.

Then, now we can infer the intrinsic velocity  $\beta_{\text{int}}$  by combining the observed brightness ratio and the core shift. Figure 8 shows an allowed range of  $\beta_{\text{int}}\text{--}i$  plane for the M 104 jet. In this plot, we adopt the continuous jet model to relate  $R$  with  $(\beta_{\text{int}} - i)$  i.e.,  $R = [(1 + \beta_{\text{int}} \cos \theta)/(1 - \beta_{\text{int}} \cos \theta)]^{2-\alpha}$  (e.g., Ghisellini et al. 1993). Here, we adopt  $\alpha = -1.1$  based on the optically-thin part of the observed jet. We found that the allowed range of the jet velocity results in  $0.02 < \beta_{\text{int}} < 0.2$  ( $1.00 < \Gamma < 1.02$ ) under the ranges of inclination angle  $1^\circ < i < 25^\circ$  and the brightness ratio  $1.1 < R < 2.1$ , implying that the M 104 jet is highly sub-relativistic. Interestingly, this jet speed of M 104 seems to be quite slower than that suggested for M 81/NGC 4258 based on their VLBI-scale properties (roughly  $\beta_{\text{int}} \gtrsim 0.9$  or  $\Gamma \gtrsim 2\text{--}3$ ; Doi et al. 2013; Falcke & Biermann 1999). Since VLBI observations of M 104 are looking at the very first stage of jet formation ( $100 R_s$  scale from the black hole) compared to those for M 81/NGC 4258 ( $10^3\text{--}4 R_s$  or more downstream region), this discrepancy could be related to some acceleration processes along the jet. Note that the suggested tendency of a smaller  $i$  with a slower  $\beta_{\text{int}}$  would become even stronger, if the observed core shift is affected by the ionospheric residuals.

The derived inclination angle of the M 104 jet has an intriguing implication for the AGN unification paradigm (Urry & Padovani 1995). The M 104 nucleus

is known to be one of the representative sources belonging to the “true type II AGN”; only narrow optical emission-line components are detected (e.g., Nicholson et al. 1998) but the amount of obscuring materials along our line-of-sight is only moderate, as indicated by X-ray studies (e.g.  $N_H = 1.8 \times 10^{21} \text{ m}^{-2}$ ; Pellegrini et al. 2003) and also by optical studies (Ho et al. 1997b). If the plane of the circumnuclear torus is perpendicular to the radio jets (such a condition seems to be actually realized for nearby AGNs; Matsushita 2012), the observed weak obscuration can be a natural consequence of less intervening material along our line-of-sight (i.e., a nearly face-on-view torus). In this case, the M 104 nucleus would actually belongs to the type I AGN instead of the type II, and thus the apparent absence/weakness of the broad line components indicates the intrinsic disappearance/weakness of the broad line region (BLR). Indeed, some theoretical studies predict the intrinsic disappearance of BLR under certain bolometric luminosities (e.g.,  $L_{\text{bol}} < 10^{41.8} (M_{\text{BH}}/10^8 M_\odot)^2 \text{ erg s}^{-1}$ ; Laor 2003), and the M 104’s low luminosity well satisfies this criteria. A face-on view of the M 104 circumnuclear torus is also suggested by the detection of silicate emission feature in the IR spectra (Shi et al. 2010).

Finally, we briefly remark a potential importance of the comparison between M 104 and M 87. While these two sources harbor the central black holes with similar masses, the powerfulness of the radio jets is remarkably different. Such a distinction may be regulated by the other fundamental parameters of black holes such as spin or/and accretion rate (Sikora et al. 2007), or physical properties of the inner part of the accretion flow. In any case, direct vicinity of the black hole is relevant. M 104 and M 87 are a unique pair for testing this issue because the black hole vicinity is actually accessible at a similar horizon-scale resolution. In particular, the use of ALMA or VLBI at mm-to-submm regime (Doeleman et al. 2012) will be the key, because at such frequencies the synchrotron emission becomes more transparent to the jet base and most of the emission comes from the closest part of the central black hole.

## 5. SUMMARY

We investigated the milliarcsecond-scale structure of the M 104 (Sombrero) nucleus with the dedicated VLBA observations. The followings are new progresses and findings;

1. We obtained the VLBI images of the M 104 nucleus, with a drastic improvement of sensitivity and resolution, at the seven frequencies between 1.4 and 43 GHz. At 15, 24 and 43 GHz, this is the first clear VLBI detection and imaging for this nucleus. At 43 GHz, we have resolved the nuclear structure down to a scale of  $\lesssim 100 R_s$  near the central engine. Along with SgrA\*, M 87 and Cen A, M 104 is the the fourth source in which such an immediate vicinity of the central black hole was imaged.
2. The innermost region (the radio core) shows a mildly inverted ( $\alpha \sim 0.14$ ) spectrum between 1.4 and 43 GHz with a brightness temperature of  $T_B \gtrsim 3 \times 10^9 \text{ K}$ . The size of the radio core is clearly frequency dependent as  $\propto \nu^{-1.20}$  with a highly elongated shape in a north-south direction. We also obtained a tendency of the core position shift toward a northern direction with decreasing frequency. These results indicate a nonthermal

process near the central engine, and are consistent with synchrotron emission in an optically-thick regime.

3. We revealed the two-sided extended structure on milliarcsecond scale, which is extending from the radio core toward northern and southern directions. This structure shows a steep spectrum with  $\alpha \sim -1.1$ . By putting together the revealed properties for the radio core and the extended structure, we conclude that the central engine of M104 is powering the nuclear radio jets, and the jets are overwhelming the radio emission from the underlying RIAF over the observed frequencies.
4. Based on the observed brightness ratio, core shift and its comparison with a theoretical expectation, we derived the following physical parameters for the M 104 jet: (1) the northern side is the approaching jet, while the southern part are receding; (2) the inclination angle of the jet is relatively close to our line-of-sight, probably less than  $\sim 25^\circ$ ; (3) the intrinsic velocity of the jets is highly sub-relativistic at a speed of  $\beta_{\text{int}} \lesssim 0.2$ .

#### APPENDIX

##### CALIBRATOR J1239–1023

J1239–1023 (1237–101) is a flat spectrum radio quasar (Healey et al. 2007) at a redshift of  $z = 0.752$  (Wisotzki et al. 2000). In Figure 9 we show a self-calibrated image of J1239–1023 taken by our VLBA observation at 15 GHz. The source structure is relatively complex with multiple bright components, so in this case the selection of a reliable reference position becomes a main concern. Fortunately, we identified a well-isolated, bright feature at  $\sim 4$  mas downstream of the jet base. This feature (we term A1) is consistently identified at all the observed frequencies, and we confirmed its optically-thin nature with a steep spectrum of  $\alpha = -0.8$  between 2 and 43 GHz. We can therefore use this feature as a reliable position reference.

Supposing that A1 has no frequency-dependent position shifts, we measured relative positions of the M 104 core with respect to the intensity centroid of this feature. At each frequency, we determined the centroid position by fitting a single Gaussian model to this feature. Position uncertainty of the centroid at each frequency was estimated by the derived Gaussian size divided by the peak-to-noise ratio (Fomalont 1999). Because A1 is sufficiently compact ( $< 1$  mas) and bright (peak-to-noise  $> 50$ ) between 2.3 and 24 GHz, the centroid positions were determined with an accuracy of  $\sim 20 \mu\text{as}$  at these frequencies. Only at 43 GHz, the feature is relatively weak. However, we can still use the brighter optically-thin components in the upstream region, which are well resolved in the images at 15, 24 and 43 GHz (A2 and A3 in Figure 9). With the help of these brighter components, we successfully made the image alignment between 22 and 43 GHz at the same level of position accuracy as that of the lower frequency data. We confirmed that no significant structural/flux changes or motions were present over the two epochs.

#### REFERENCES

- Anderson, J. M., Ulvestad, J. S., & Ho, L. C. 2004, *ApJ*, 603, 42
- Bajaja, E., Dettmar, R. J., Hummel, E., Wielebinski, R. 1988, *A&A*, 202, 35
- Bendo, G. J., Buckalew, B. A., Dale, D. A., Draine, B. T., Joseph, R. D., et al. 2006, *ApJ*, 645, 134
- Bietenholz, M. F., Bartel, N., & Rupen, M. P. 1996, *ApJ*, 457, 604
- Bietenholz, M. F., Bartel, N., & Rupen, M. P. 2000, *ApJ*, 532, 895
- Bietenholz, M. F., Bartel, N., & Rupen, M. P. 2004, *ApJ*, 615, 173
- Blandford, R. D., & Begelman, M. C. 1999, *MNRAS*, 303, L1
- Bontempi, P., Giroletti, M., Panessa, F., Orienti, M., & Doi, A. 2012, *MNRAS*, 426, 588
- de Bruyn, A. G., Crane, P. C., Price, R. M., & Carlson, J. B. 1976, *A&A*, 46, 243
- Deller, A. T., Briske, W. F., Phillips, C. J., et al. 2011, *PASP*, 123, 275
- Di Matteo, T., Carilli, C. L., Fabian, A. C. 2001, *ApJ*, 547, 731
- Doeleman, S. S., Weintroub, J., Rogers, A. E. E., Plambeck, R., Freund, R., et al. 2008, *Nature*, 455, 78
- Doeleman, S. S., Fish, V. L., Schenck, D. E., Beaudoin, C., Blundell, R., et al. 2012, *Science*, 338, 355
- Doi, A., Kamenno, S., Kohno, K., Nakanishi, K., & Inoue, M. 2005, *MNRAS*, 363, 692
- Doi, A., et al. 2009, in *ASP Conf. Ser. 402, Approaching Micro-Arcsecond Resolution with VSOP-2*, ed. Y. Hagiwara, E. Fomalont, M. Tsuboi, & Y. Murata (San Francisco, CA: ASP), 284
- Doi, A., Nakanishi, K., Nagai, H., Kohno, K., & Kamenno, S. 2011, *AJ*, 142, 167
- Doi, A., Kohno, K., Nakanishi, K., Kamenno, S., Inoue, M., et al. 2013, *ApJ*, 765, 63
- Falcke, H., Biermann, P. L. 1995, *A&A*, 293, 665
- Falcke, H., Biermann, P. L. 1999, *A&A*, 342, 49 (FB99)
- Falcke, H., Nagar, N. M., Wilson, S., & Ulvestad, J. S. 2000, *ApJ*, 542, 197
- Fomalont, E. B. 1999, in *ASP Conf. Ser. 180, Synthesis Imaging in Radio Astronomy II*, ed. G. B. Taylor, C. L. Carilli, & R. A. Perley (San Francisco, CA: ASP), 301
- Ghisellini, G., Padovani, P., Celotti, A., & Maraschi, L. 1993, *ApJ*, 407, 65
- Giroletti, M., Taylor, G. B., Giovannini, G. 2005, *ApJ*, 622, 178
- Giroletti, M., & Panessa, F. 2009, *ApJ*, 706, L260
- Graham, D. A., Weiler, K. W., Wielebinski, R. 1981, *A&A*, 97, 388
- Gordon, D. 2005, in *ASP Conf. Ser. 340, Future Directions in High Resolution Astronomy: The 10th Anniversary of the VLBA*, ed. J. Romney & M. Reid (San Francisco, CA: ASP), 496
- Hada, K., Doi, A., Kino, M., Nagai, H., Hagiwara, Y., et al. 2011, *Nature*, 477, 185
- Healey, S. E., Romani, R. W., Taylor, G. B., Sadler, E. M., Ricci, R., et al. 2007, *ApJS*, 171, 61
- Heckman, T. M. 1980, *A&A*, 87, 152
- Herrnstein, J. R., Moran, J. M., Greenhill, L. J., Diamond, P. J., Miyoshi, M., et al. 1997, *ApJ*, 475, L17
- Ho, L. C., Filippenko, A., & Sargent, W. L. W. 1997, *ApJ*, 487, 568 (Ho et al. 1997a)
- Ho, L. C., Filippenko, A., Alexei, V., & Sargent, W. L. W. 1997, *ApJS*, 112, 315 (Ho et al. 1997b)

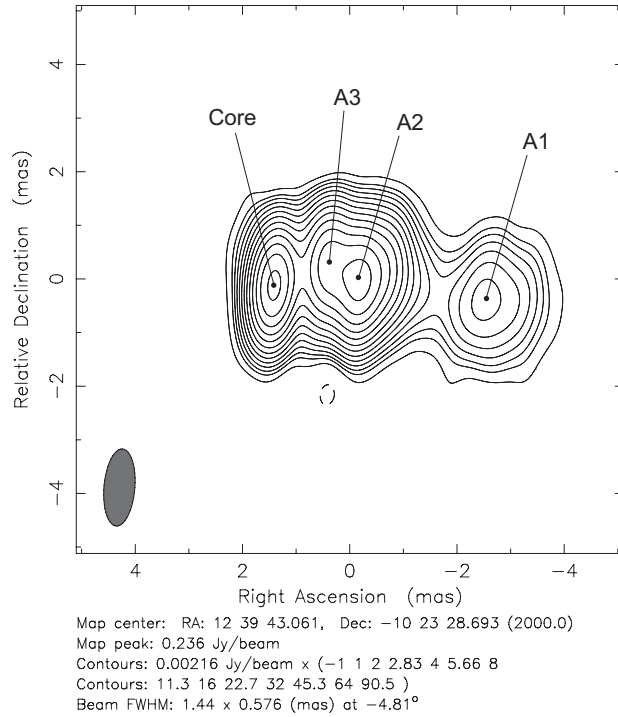


FIG. 9.— Self-calibrated image of J1239–1023 taken by our VLBA observations at 15 GHz. Contours start from  $-1, 1, 2, \dots$  times  $0.2 \text{ mJy/beam}$  ( $3\sigma$  image rms level) and increasing by factors of  $2^{1/2}$ . We identified the easternmost feature to be the radio core at the jet base because of the observed optically-thick spectrum at the lower frequency side. We used a bright, well-isolated knot A1 as a position reference for the astrometry of M 104. At 15, 24 and 43 GHz, we also identified additional bright features A2 and A3, both of which shows optically-thin spectra at these frequencies. We additionally used these features when aligning the images between 24 and 43 GHz.

- Ho, L. 1999, *ApJ*, 516, 672  
 Ho, L. C. 2008, *ARA&A*, 46, 475  
 Horiuchi, S., Meier, D. L., Preston, R. A., & Tingay, S. J. 2006, *PASJ*, 58, 211  
 Hummel, E., van der Hulst, J. M., & Dickey J. M. 1984, *A&A*, 134, 207  
 Junor, W., Biretta, J. A., & Livio, M. 1999, *Nature*, 401, 891  
 Königl, A. 1981, *ApJ*, 243, 700  
 Kormendy, J., et al. 1996, *ApJ*, 473, L91  
 Kormendy, J. 1988, *ApJ*, 335, 40  
 Kovalev, Y. Y., Lobanov, A. P., Pushkarev, A. B., & Zensus, J. A. 2008, *A&A*, 483, 759  
 Krause, M., Wielebinski, R., & Dumke, M. 2006, *A&A*, 327, 499  
 Krichbaum, T. P., Graham, D. A., Bremer, M., et al. 2006, *JPhCS*, 54, 328  
 Laor, A. 2003, *ApJ*, 590, 86  
 Liu, H., & Wu, Q. 2013, *ApJ*, 764, 17L  
 Lo, K. Y., Backer, D. C., Kellermann, K. I., Reid, M., Zhao, J. H., et al. 1993, *Nature*, 362, 38  
 Lobanov, A. P. 1998, *A&A*, 330, 79  
 Lu, R.-S., Krichbaum, T. P., Eckart, A., Křůň, S., Kunneriath, D., et al. 2011, *A&A*, 525, 76  
 Ly, C., Walker, R. C., & Junor, W. 2007, *ApJ*, 660, 200  
 Mahadevan, R. 1997, *ApJ*, 477, 585  
 Manmoto, T., Mineshige, S., & Kusunose, M. 1997, *ApJ*, 489, 791  
 Marconi, A., Capetti, A., Axon, D. J., Koekemoer, A., Macchetto, D., et al. 2001, *ApJ*, 549, 915  
 Markoff, S., et al. 2008, *ApJ*, 681, 905  
 Martí-Vidal, I., Marcaide, J. M., Alberdi, A., Pérez-Torres, M. A., Ros, E., et al. 2011, *A&A*, 533, 111  
 Matsushita, S. 2012, *JPhCS*, 372, 2043  
 Müller, C., Kadler, M., Ojha, R., Wilms, J., Böck, M., et al. 2011, *A&A*, 530, 11  
 Nagar, N. M., Wilson, A. S., & Falcke, H., 2001, *ApJ*, 559, 87  
 Nagar, N. M., Falcke, H., Wilson, S., & Ulvestad, J. S. 2002, *A&A*, 392, 53  
 Nagar, N. M., Falcke, H., & Wilson, S. 2005, *A&A*, 435, 521  
 Narayan, R., & Yi, I., 1994, *ApJ*, 428, 13  
 Narayan, R., & Yi, I., 1995, *ApJ*, 452, 710  
 Narayan, R., Mahadevan, R., Grindlay, J. E., Popham, R. G., & Gammie, C. 1998, *ApJ*, 492, 554  
 Narayan, R., Igumenshchev, I. V., & Abramowicz, M. A. 2000, *ApJ*, 539, 798  
 Narayan, R., Sadowski, A., Penna, R. F., & Kulkarni, A. K. 2012, *MNRAS*, 426, 3241  
 Neumayer, N. 2010, *PASA*, 27, 449  
 Nicholson, K. L., Reichert, G. A., Mason, K. O., Puchnarewicz, E. M., Ho, L. C., et al. 1998, *MNRAS*, 300, 893  
 Pellegrini, S., Baldi, A., Fabbiano, G., & Kim, D.-W. 2003, *ApJ*, 597, 175  
 Preston, R. A., et al. 1985, *AJ*, 90, 1599  
 Quataert, E., & Narayan, R. 1999, *ApJ*, 520, 298  
 Quataert, E., Di Matteo, T., Narayan, R., & Ho, L. C. 1999, *ApJ*, 525, 89  
 Ros, E., Pérez-Torres, M. A. 2012, *A&A*, 537, 93  
 Rubin, V. C., Burstein, D., Ford, W. K., Jr., and Thonnard, N. 1985, *ApJ*, 289, 81  
 Shaffer, D. B., & Marscher, A. P. 1979, *ApJ*, 233, L105  
 Shen, Z.-Q., Lo, K. Y., Liang, M.-C., Ho, P. T. P., & Zhao, J.-H. 2005, *Nature*, 438, 62  
 Shepherd, M. C. 1997, in *ASP Conf. Ser. 125, Astronomical Data Analysis Software and Systems VI*, ed. G. Hunt & H. E. Payne (San Francisco, CA: ASP), 77  
 Shi, Y., et al. 2010, *ApJ*, 714, 115  
 Sikora, M., Stawarz, L., & Lasota, J.-P. 2007, *ApJ*, 658, 815  
 Sokolovsky, K. V., Kovalev, Y. Y., Pushkarev, A. B., & Lobanov, A. P. 2011, *A&A*, 532, 38  
 Spitler, L. R., Larsen, S. S., Strader, J., et al. 2006, *AJ*, 132, 1593  
 Tingay, S. J., Jauncey, D. L., Reynolds, J. E., Tzioumis, A. K., King, E. A., et al. 1998, *AJ*, 115, 960  
 Ulvestad, J. S., & Ho, L. C. 2001, *ApJ*, 562, L133  
 Urry, C. M., & Padovani, P. 1995, *PASP*, 107, 803  
 Wisotzki, L., Christlieb, N., Bade, N., Beckmann, V., Köhler, T., et al. 2000, *A&A*, 358, 77  
 Yuan, F., Markoff, S., Falcke, H. 2002, *A&A*, 383, 854  
 Yuan, F., Quataert, E., & Narayan, R. 2003, *ApJ*, 598, 301  
 Yuan, F., Yu, Z., & Ho, L. C. 2009, *ApJ*, 703, 1034  
 Yuan, F., Bu, D., & Wu, M. 2012, *ApJ*, 761, 130